Many-body renormalization of the electron effective mass of InSe

Wenbin Li and Feliciano Giustino

Phys. Rev. B **101**, 035201 — Published 13 January 2020

DOI: 10.1103/PhysRevB.101.035201

Many-body renormalization of the electron effective mass of InSe

Wenbin Li[1,2] and Feliciano Giustino[3,4,2,*]

[1] *School of Engineering, Westlake University, Hangzhou 310024, China*
[2] *Department of Materials, University of Oxford, Parks Road OX1 3PH, Oxford, United Kingdom*
[3] *Oden Institute for Computational Engineering & Sciences, The University of Texas at Austin, Austin, Texas 78712, USA*
[4] *Department of Physics, The University of Texas at Austin, Austin, Texas 78712, USA*

(Dated: January 2, 2020)

The layered semiconductor InSe has a wide range of attractive electronic and optoelectronic properties, in which the effective mass of the charge carriers plays a key role. Here, we study from first principles the many-body renormalization of the electron effective mass in γ-InSe, taking into account the effects of both electron-electron and electron-phonon interactions. Electron-electron interaction, treated within the many-body GW approximation, leads to around 15% of increase in the in-plane effective mass over the result from density functional theory, and a more than threefold increase in the out-of-plane electron effective mass. The surprisingly large directional anisotropy in the mass renormalization is explained in terms of the symmetries of band-edge wavefunctions. The mass enhancement induced by electron-phonon interactions, which we find to mainly originate from Fröhlich electron-phonon coupling, is less than 10% at room temperature, indicating weak polaronic effect. After including the many-body renormalization effects, the calculated electron effective masses of InSe are 0.12 and 0.09 in the in-plane and out-of-plane directions, respectively.

I. INTRODUCTION

With a measured room temperature electron mobility exceeding 1000 cm^2/Vs in multilayer samples, InSe has recently emerged as a promising layered semiconductor for a new generation of high-performance, energy-efficient, and flexible electronics [1–9]. Such a large carrier mobility in bulk and multilayer systems has been confirmed by recent calculations based on the *ab initio* Boltzmann transport equation approach [10]. The large carrier mobility of multilayer InSe can be explained in part by the small electron effective mass (m^*) of InSe, which was experimentally determined to be around $0.14m_e$ and $0.08m_e$ along the in-plane and out-of-plane directions respectively [11], where m_e represents the rest mass of an electron. Density functional theory (DFT) calculations within the local density approximation [12–14], on the other hand, give the corresponding in-plane and out-of-plane effective masses to be $0.10m_e$ and $0.024m_e$, respectively [10]. The discrepancy between the DFT and experimental results raises the interesting question of how the electron effective masses of InSe are renormalized by the many-body interactions in the material.

Many-body interactions in the forms of electron-electron interaction (EEI) and electron-phonon interaction (EPI) can both strongly renormalize the effective mass of charge carriers in solids [15–17]. The consideration of both EEI and EPI is therefore needed for an accurate determination of carrier effective mass, and the corresponding mass renormalization provides insights into the nature and strength of many-body interactions in a solid. The influence of many-body interactions on the carrier effective mass of InSe is so far not well understood. In this work, we employ state-of-the-art first-principles computational methodologies based on many-body perturbation theory to calculate the effective mass enhancement of InSe that arises from both EEI and EPI.

We find strong directional anisotropy in the electron effective mass renormalization by EEI. The EEI-induced electron effective mass enhancement in the out-of-plane direction is more than an order of magnitude larger than the mass enhancement in the in-plane direction (more than threefold versus 15%), which is closely related to the symmetry of band-edge wavefunctions. Furthermore, we find less than 10% of EPI-induced electron effective mass enhancement in both the in-plane and out-of-plane directions at room temperature. This effect originates from the weak Fröhlich coupling that dominates the EPI in the system.

The paper is organized as follows. In Sec. II we describe the computational methodology for the calculations of the EEI and EPI in InSe. Sec. III presents the main results, including the effects of both EEI and EPI on the electron effective mass renormalization. In Sec. IV we discuss our calculation results in relation to experimental measured electron effective mass of InSe. In Sec. V we summarize our key findings and present the conclusions.

II. METHODOLOGY

The atomistic structure of γ-InSe is shown in Fig. 1(a). Each monolayer of InSe has a hexagonal lattice with point group symmetry C_{3v}, in which two atomic layers of indium are sandwiched between two selenium layers, as illustrated in Fig. 1(b). In bulk γ-InSe, monolayers stack vertically such that the In sublattice of a given

* fgiustino@oden.utexas.edu

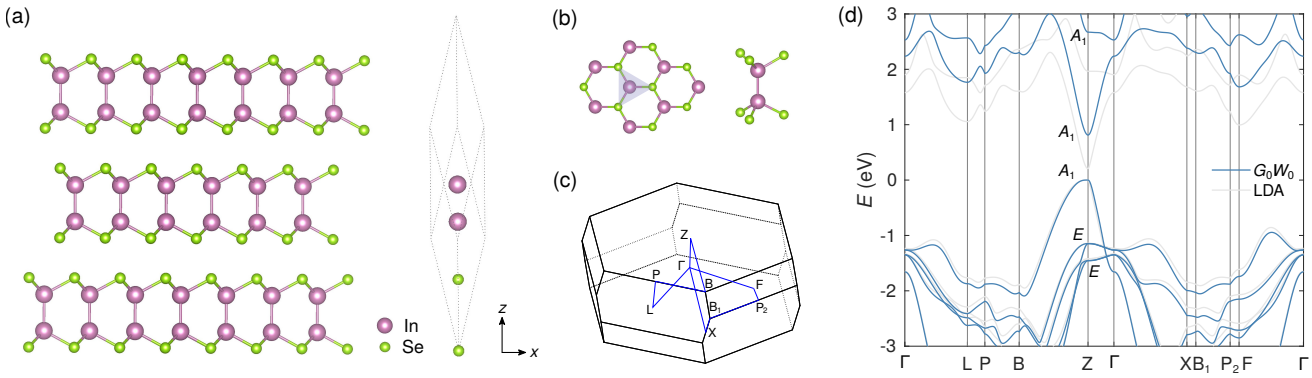

FIG. 1. The atomistic model and electronic band structure of γ-InSe. (a) Side view of the structural model, showing the layer stacking sequence of the bulk. The rhombohedral unit cell is shown alongside, and the in- and out-of-plane directions are indicated. (b) Top view of InSe monolayer and a trigonal-prismatic structural unit in the monolayer. The latter corresponds to the shaded region on the top view of the monolayer structure. (c) The first Brillouin zone corresponding to the rhombohedral unit cell. (d) The electronic band structures from many-body G_0W_0 calculation, as well as density functional theory (DFT) calculation within the local density approximation (LDA). The G_0W_0 and DFT-LDA results are represented by blue and gray lines respectively. The zero of energy corresponds to the energy maximum of the valence band.

layer sits on top of the Se sublattice that belongs to the layer below. The monolayers are held together by weak dispersive forces. Different layer stacking geometries can lead to different structural polymorphs, such as the β and ε phases [18]. The most commonly observed phases of InSe are the γ and β phases, and their electronic and transport properties were previously found to be rather similar [10]. The smallest translationally invariant unit of γ-InSe can be chosen to be a rhombohedral primitive cell with two In and two Se atoms, as shown in Fig. 1(a).

We obtain the electronic structure of InSe by using DFT [12] and subsequently calculate the quasiparticle band structures renormalized by both EEI and EPI. The EEI is treated using many-body perturbation theory in the GW approximation [19, 20], while the effect of EPI is included by calculating the Fan-Migdal electron self-energy due to EPI [17, 21, 22]. Details of the DFT, GW, and electron-phonon calculations are presented below. The effective mass tensor of InSe is subsequently obtained from the DFT and quasiparticle band structures by calculating the second derivative of band-edge energies E with respect to the wavevecor $\mathbf{k}$ as $m^*_{ij} = \hbar^2(\partial^2 E/\partial k_i \partial k_j)^{-1}$. We focus on the effective mass of the electrons in the conduction band as the electron mobility of InSe is much higher than the hole mobility [10], making the electron effective mass a primary subject of interest in many practical applications.

A. DFT calculations

DFT calculations of bulk γ-InSe are carried out within the local density approximation (LDA) [14] as implemented in the Quantum ESPRESSO code [23]. For the DFT calculations we use the experimental lattice constants of γ-InSe as reported in Ref. 24, and perform structural optimization of the internal atomic coordinates, with a force convergence criterion of 10^{-5} Ry/Bohr. We use the norm-conserving pseudopotentials of the Troullier–Martins form [25], treating the semicore In $4d$ electrons as valence electrons. A plain-wave cutoff energy of 100 Ry is used to expand the electronic wavefunctions. The Brillouin zone is sampled using a shifted $8\times8\times8$ $\mathbf{k}$-point mesh. Spin-orbit coupling (SOC) is not included as the effect of SOC on the dispersion of the conduction band edge is insignificant [10].

B. GW calculations

On top of the DFT band structure, we calculate the quasiparticle band dispersion of InSe within GW many-body perturbation theory [19, 20], as implemented in the Yambo code [26]. The GW self-energy is evaluated in the G_0W_0 approximation as $\Sigma = iG_0W_0$, where G_0 denotes the electron Green's function calculated from the DFT Kohn-Sham eigenfunctions $\psi_{n\mathbf{k}}$ and eigenvalues $\epsilon_{n\mathbf{k}}$ corresponding to the band index n and the wavevector $\mathbf{k}$. The screened Coulomb interaction W_0 is evaluated using the random phase approximation [16, 27]. The frequency dependence of the dielectric matrix in the evaluation of W_0 is calculated using the Godby-Needs plasmon-pole model [28]. The renormalized GW quasiparticle energies $E_{n\mathbf{k}}$ are related to the DFT eigenvalues $\epsilon_{n\mathbf{k}}$ as [16]:

$$E_{n\mathbf{k}} = \epsilon_{n\mathbf{k}} + Z^{\mathrm{EEI}}_{n\mathbf{k}} \langle \psi_{n\mathbf{k}} | \Sigma(\epsilon_{n\mathbf{k}}) - V_{xc} | \psi_{n\mathbf{k}} \rangle, \qquad (1)$$

where $Z^{\mathrm{EEI}}_{n\mathbf{k}}$ is the quasiparticle renormalization factor associated with EEI, and V_{xc} denotes the exchange-correlation potential.

For the G_0W_0 calculations of the quasiparticle energies we use a 60 Ry plane-wave cutoff for the exchange self-energy, a 15 Ry cutoff for the polarizability, 500 bands,

and the terminator technique of Ref. 29 for accelerated convergence with respect to the number of bands. These parameters are sufficient to converge the quasiparticle energy within 0.05 eV. The G_0W_0 quasiparticle energies are calculated on a Γ-centered 6×6×6 grid, and are subsequently interpolated on an arbitrary **k**-mesh using Wannier interpolation [30]. We note that our calculations are for bulk InSe and therefore do not involve the convergence issues unique to the *GW* calculations of 2D materials [31, 32].

C. Electron-phonon calculations

For the calculation of the EPI-renormalized effective mass we use the EPW code [33]. Starting from the G_0W_0 electronic band structure, we calculate the Fan-Migdal electron self-energy $\Sigma_{n\mathbf{k}}$ at electron energy ε and temperature T as [17, 21, 22]:

$$\Sigma_{n\mathbf{k}}(\varepsilon;T) = \sum_{m\nu}\int \frac{d\mathbf{q}}{\Omega_{\mathrm{BZ}}}|g_{mn\nu}(\mathbf{k},\mathbf{q})|^2 \times \sum_{\pm}\frac{n_{\mathbf{q}\nu}+(1\pm[2f_{m\mathbf{k}+\mathbf{q}}-1])/2}{\varepsilon-\varepsilon_{m\mathbf{k}+\mathbf{q}}\pm\hbar\omega_{\mathbf{q}\nu}-i\delta}. \quad (2)$$

Here, $\varepsilon_{m\mathbf{k}}$ denotes the energy of the band m and wavevector $\mathbf{k}$, $\omega_{\mathbf{q}\nu}$ represents the vibrational frequency for the phonon branch ν and wavevector $\mathbf{q}$, $g_{mn\nu}(\mathbf{k},\mathbf{q})$ are the electron-phonon matrix elements, and the integral is carried out over the first Brillouin zone whose volume is Ω_{BZ}. The effect of temperature is included through the phonon occupation number $n_{\mathbf{q}\nu}$ and the Fermi-Dirac distribution function $f_{n\mathbf{k}}$ of the electrons.

The electron-phonon matrix elements $g_{mn\nu}(\mathbf{k},\mathbf{q})$ are initially calculated on a 6×6×6 grid for both the electron and phonon wavevectors using the Quantum ESPRESSO code [23], and subsequently interpolated onto fine grids using the Wannier interpolation implemented in Wannier90 and EPW [30, 33, 34]. The dielectric constants and Born effective charges are calculated using density functional perturbation theory [35]. Both shifted and unshifted Monkhorst-Pack meshes up to $28\times28\times28$ are used to obtain converged results. The converged values are used for the interpolation of Fröhlich electron-phonon matrix elements [36]. Brillouin zone integration in the electron-phonon self-energy is carried out by sampling the phonon wavevector $\mathbf{q}$ according to a random Cauchy distribution centered at Γ point, with the weight of each $\mathbf{q}$ point determined by its Voronoi volume. More than one million $\mathbf{q}$ points are used for the Brillouin-zone integration. In our calculations of effective mass enhancement, the Debye-Waller contribution is not included as the Debye-Waller self-energy varies smoothly as a function of $\mathbf{k}$ within the same band [17], and therefore it can be neglected in the effective mass calculation [37].

Using the expression for electron-phonon self-energy in Eq. (2), we calculate the EPI-renormalized quasiparticle energies using the Brillouin-Wigner perturbation theory [17] as:

$$\mathcal{E}_{n\mathbf{k}} = \varepsilon_{n\mathbf{k}} + Z^{\mathrm{EPI}}_{n\mathbf{k}}\mathrm{Re}\Sigma_{n\mathbf{k}}(\varepsilon_{n\mathbf{k}}), \quad (3)$$

where $\mathcal{E}_{n\mathbf{k}}$ is the EPI-renormalized quasiparticle energy, $\mathrm{Re}\Sigma_{n\mathbf{k}}(\varepsilon_{n\mathbf{k}})$ the real part of the Fan-Migdal electron self-energy, and $Z^{\mathrm{EPI}}_{n\mathbf{k}} = [1-\mathrm{Re}(\partial\Sigma_{n\mathbf{k}}/\partial\varepsilon)|_{\varepsilon_{n\mathbf{k}}}]^{-1}$ is the quasiparticle renormalization factor associated with the EPI. By making the approximation $Z^{\mathrm{EPI}}_{n\mathbf{k}} = 1$, the Rayleigh-Schrödinger approach is obtained. The EPI-renormalized effective mass is then calculated from the second derivative of $\mathcal{E}_{n\mathbf{k}}$ with respect to $\mathbf{k}$. Denoting by $m^{\mathrm{QP},*}$ and m^* the EPI-renormalized effective mass and the G_0W_0 effective mass respectively, the effective mass enhancement parameter λ associated with EPI is calculated through the relation $m^{\mathrm{QP},*} = m^*(1+\lambda)$.

TABLE I. The bandgap (E_g), in-plane effective mass (m^*_{xx}), and out-of-plane effective mass (m^*_{zz}) of γ-InSe obtained from DFT and G_0W_0 calculations. The effective masses are measured in units of m_e, which represents the rest mass of an electron.

	E_g (eV)	m^*_{xx}/m_e	m^*_{zz}/m_e
DFT	0.21	0.103	0.024
G_0W_0	0.81	0.118	0.086

III. RESULTS

A. Effective mass renormalization by electron-electron interactions

Fig. 1d shows the calculated G_0W_0 quasiparticle band structure of γ-InSe together with the DFT band structure. The calculated DFT and G_0W_0 bandgaps (E_g) as well as the in- and out-of-plane electron effective masses (denoted by m^*_{xx} and m^*_{zz} respectively) are listed in Table I. The inclusion of many-body EEI in the G_0W_0 approximation leads to an increase of E_g from 0.21 to 0.81 eV, which is accompanied by increases of both m^*_{xx} and m^*_{zz}. However, a significant difference exists in the magnitude of mass enhancement between in- and out-of-plane directions. The inclusion of EEI results in an increase of the in-plane effective mass m^*_{xx} by 15%, from 0.103 to 0.118. In contrast, the out-of-plane effective mass m^*_{zz} increases by more than 350%, from 0.024 to 0.086.

We find that the surprisingly large directional anisotropy in the mass enhancement of γ-InSe by EEI can be explained using $\mathbf{k}\cdot\mathbf{p}$ perturbation theory. Within the theory, the effective mass of the conduction-band electrons can be written as [38]:

$$\frac{m_e}{m^*_{ij}} = \delta_{ij} + \frac{2}{m_e}\sum_{m\neq c}\frac{\langle\psi_c|p_i|\psi_m\rangle\langle\psi_m|p_j|\psi_c\rangle}{E_c-E_m}, \quad (4)$$

where δ_{ij} denotes the Kronecker delta, and the summation is over the band index m but excludes the lowest con-

TABLE II. Character table of the C_{3v} point group. The three symmetry classes of the point-symmetry group are identity (E), two three-fold rotations (C_{3v}), and three vertical mirror planes parallel to the threefold axis (σ_v). The three irreducible representations are denoted by A_1, A_2, and E.

C_{3v}	E	$2C_3$	$3\sigma_v$
A_1	+1	+1	+1
A_2	+1	+1	−1
E	+2	−1	0

duction band labelled as c. The Bloch wavefunctions and the corresponding band energies at the crystal momentum corresponding to the conduction-band minimum, i.e. the Z point in the first Brillouin zone, are denoted by $|\psi_m\rangle$ and E_m, respectively. p_i represents the component of the momentum operator. Based on Eq. (4), the in- and out-of-plane effective mass can be written respectively as:

$$\frac{m_e}{m^*_{xx}} = 1 + \frac{2}{m_e}\sum_{m\neq c}\frac{|\langle\psi_m|p_x|\psi_c\rangle|^2}{E_c - E_m}, \tag{5}$$

$$\frac{m_e}{m^*_{zz}} = 1 + \frac{2}{m_e}\sum_{m\neq c}\frac{|\langle\psi_m|p_z|\psi_c\rangle|^2}{E_c - E_m}. \tag{6}$$

These equations indicate that only the states $|\psi_m\rangle$ that are energetically close to the conduction band-minimum state $|\psi_c\rangle$ and which have non-zero momentum matrix elements $\langle\psi_m|p_i|\psi_c\rangle$ will have a significant influence on the electron effective mass. These states can be deduced from group-theoretical considerations of the symmetry of the wavefunctions.

Bulk γ-InSe has a point group symmetry C_{3v} with respect to either Se or In atoms. The small-group of the wavevector at Z is also C_{3v}. The Bloch wavefunctions at Z can therefore be classified according to the three irreducible representations of the C_{3v} group, which are denoted by A_1, A_2, and E. The corresponding character table of the C_{3v} point group is shown in Table II.

In Fig. 1(d) we label the symmetry representations of the wavefunctions at Z. By analyzing the wavefunctions and their transformations under symmetry operations, we find that both the valence and conduction band-edge states, represented by $|\psi_v\rangle$ and $|\psi_c\rangle$ respectively, derive from the s and p_z orbitals of In/Se atoms and belong to the A_1 representation. On the other hand, the four valence-band wavefunctions at Z below the topmost valence band, which are separated into two subgroups due to their two-fold degeneracy, derive from the p_x/p_y orbitals of In/Se atoms and belong to the E representation. In the C_{3v} group, the momentum operators p_x and p_z transform as E and A_1 respectively. Therefore, according to the direct product relationships $E \otimes A_1 = E$ and $A_1 \otimes A_1 = A_1$ [39], $p_x|\psi_c\rangle$ transforms as E, and $p_z|\psi_c\rangle$ transforms as A_1. It then follows from group theory that the matrix element $\langle\psi_m|p_x|\psi_c\rangle$ is non-zero only when $|\psi_m\rangle$ belongs to the irreducible representation E, and $\langle\psi_m|p_z|\psi_c\rangle$ is non-zero only when $|\psi_m\rangle$ belongs to the irreducible representation A_1.

The above symmetry selection rules lead to the conclusion that $\langle\psi_v|p_x|\psi_c\rangle = 0$ and $\langle\psi_v|p_z|\psi_c\rangle \neq 0$. On the other hand, opposite results hold for the momentum matrix elements between $|\psi_c\rangle$ and the four states below $|\psi_v\rangle$ at Z. Our explicit calculations of the momentum matrix elements based on the DFT wavefunctions confirm the above results. Furthermore, the results indicate that $\langle\psi_{v-1}|p_x|\psi_c\rangle$ and $\langle\psi_{v-2}|p_x|\psi_c\rangle$ are the dominant p_x matrix elements, where $|\psi_{v-1}\rangle$ and $|\psi_{v-2}\rangle$ represent the two energy-degenerate states below $|\psi_v\rangle$ respectively. These results allow us to write the expressions for the in- and out-of-plane effective mass as:

$$\frac{m_e}{m^*_{xx}} \approx 1 + \frac{2}{m_e}\frac{|\langle\psi_{v-1}|p_x|\psi_c\rangle|^2 + |\langle\psi_{v-2}|p_x|\psi_c\rangle|^2}{E_g + \Delta E_{v,v-1}}, \tag{7}$$

$$\frac{m_e}{m^*_{zz}} \approx 1 + \frac{2}{m_e}\frac{|\langle\psi_v|p_z|\psi_c\rangle|^2}{E_g}, \tag{8}$$

where $\Delta E_{v,v-1} = E_v - E_{v-1}$ represents the energy difference between $|\psi_v\rangle$ and $|\psi_{v-1}\rangle$. Our DFT and G_0W_0 calculations give very close values of $\Delta E_{v,v-1}$, both of which are around 1.1 eV. On the other hand, the DFT and G_0W_0 bandgaps, with E_g equal to 0.21 eV and 0.81 eV respectively, exhibit a much larger difference and are both smaller than $\Delta E_{v,v-1}$. Comparing the demoninators on the right-hand side of Eq. (7) and Eq. (8), it is clear that m^*_{zz} will be affected more by a change in the bandgap induced by EEI than m^*_{xx}. Using the DFT effective mass data listed in Table I, as well as the calculated values of E_g and $\Delta E_{v,v-1}$, we determine from Eq. (7) and Eq. (8) that the EEI-induced change in E_g would lead to 39% and 395% of increases in m^*_{xx} and m^*_{zz}, respectively. The one order of magnitude difference in the effective mass renormalization between m^*_{xx} and m^*_{zz} is consistent with the direct calculation result that the in-plane effective mass m^*_{xx} increases by 15% from DFT to G_0W_0, whereas the out-of-plane effective mass m^*_{xx} increases by more than 350%.

B. Effective mass renormalization by electron-phonon interactions

With the above insight into the influence of EEI on the electron effective mass of InSe, we now investigate the effective mass renormalization by EPI. Fig. 2 shows the calculated electron effective mass enhancement with respect to the G_0W_0 effective mass as a function of temperature, for both the in- and out-of-plane components of the effective mass tensor. The effective mass renormalization increases with temperature, which can be rationalized by the stronger EPI at higher temperature due to the increased phonon occupation number. The Brillouin-Wigner perturbation theory results in smaller mass enhancements than those from the Rayleigh-Schrödinger perturbation theory, consistent with a previous study of

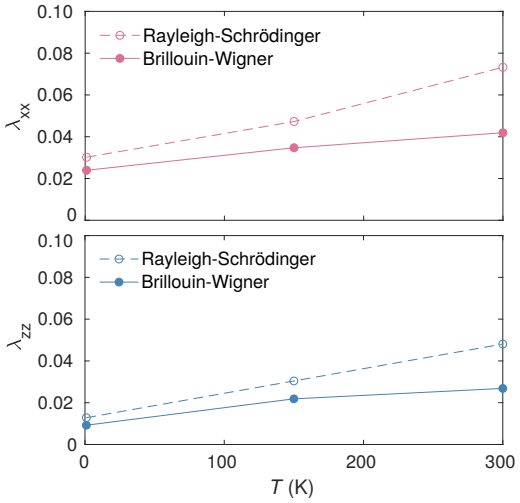

FIG. 2. Electron effective mass enhancement of γ-InSe induced by EPI. The in- and out-of-plane effective mass enhancements are calculated as a function of temperature (T) using both Rayleigh-Schrödinger and Brillouin-Wigner perturbation theory. Top panel: in-plane electron mass enhancement (λ_{xx}). Bottom panel: out-of-plane mass enhancement (λ_{zz}).

TABLE III. EPI-induced effective mass renormalization of γ-InSe at 300 K. The mass enhancement is calculated with respect to the G_0W_0 effective mass.

	In-plane		Out-of-plane	
	m^*_{xx}/m_e	λ_{xx}	m^*_{zz}/m_e	λ_{zz}
G_0W_0	0.118	–	0.086	–
Brillouin-Wigner	0.123	0.042	0.089	0.027
Rayleigh-Shrödinger	0.126	0.073	0.090	0.048

EPI-induced mass enhancement in a hybrid halide perovskite [37].

The renormalized electron effective masses at 300 K are listed in Table III. It can be seen that the EPI-induced mass enhancement is small at room temperature. For the in-plane effective mass enhancement λ_{xx}, the calculated values are around 0.04 and 0.07 using the Brillouin-Wigner and Rayleigh-Schrödinger perturbation theory, respectively. The corresponding out-of-plane mass enhancement λ_{zz} is even smaller, around 0.03 and 0.05 respectively. These numbers indicate weak polaronic mass enhancement for the electron carriers in γ-InSe, which is beneficial for device applications.

To better understand the origin of the weak EPI-induced mass enhancement, we decompose the mass enhancement into contributions from different phonon modes. Based on Eq. (2) and Eq. (3), the EPI-renormalized quasiparticle energies within the Rayleigh-Schrödinger perturbation theory can be written as:

$$\mathcal{E}_{n\mathbf{k}} = \varepsilon_{n\mathbf{k}} + \sum_{\nu} \mathrm{Re}\Sigma^{\nu}_{n\mathbf{k}}(\varepsilon_{n\mathbf{k}}), \tag{9}$$

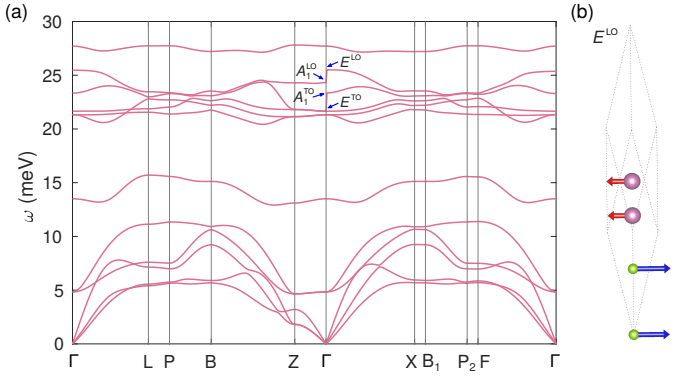

FIG. 3. Calculated phonon spectrum of γ-InSe. The phonons that exhibit LO-TO splitting are indicated by arrows in (a). The representative pattern of atomic displacements corresponding to the in-plane Fröhlich phonons are illustrated in (b).

where the summation is over the phonon branch index ν, and $\mathrm{Re}\Sigma^{\nu}_{n\mathbf{k}}(\varepsilon_{n\mathbf{k}})$ represents the real-part of the Fan-Migdal electron-phonon self-energy originated from the coupling of electron $n\mathbf{k}$ with the ν-th phonon branch. $\mathrm{Re}\Sigma^{\nu}_{n\mathbf{k}}(\varepsilon_{n\mathbf{k}})$ involves an integral over the phonon wavevector $\mathbf{q}$:

$$\mathrm{Re}\Sigma^{\nu}_{n\mathbf{k}}(\varepsilon_{n\mathbf{k}}) = \int \frac{d\mathbf{q}}{\Omega_{\mathrm{BZ}}} \sum_{m} \Bigg[|g_{mn\nu}(\mathbf{k},\mathbf{q})|^2 \times \sum_{\pm} \frac{n_{\mathbf{q}\nu} + (1 \pm [2f_{m\mathbf{k}+\mathbf{q}} - 1])/2}{\varepsilon_{n\mathbf{k}} - \varepsilon_{m\mathbf{k}+\mathbf{q}} \pm \hbar\omega_{\mathbf{q}\nu}} \Bigg]. \tag{10}$$

As described in Sec. II C, the EPI-renormalized electron effective mass $m^{\mathrm{QP},*}_{ij}$ is calculated from the second derivative of $\mathcal{E}_{n\mathbf{k}}$ with respect to $\mathbf{k}$ as $m^{\mathrm{QP},*}_{ij} = \hbar^2 \left(\partial^2 \mathcal{E}_{n\mathbf{k}}/\partial k_i \partial k_j\right)^{-1}$, and the mass enhancement factor λ_{ij} is calculated through $m^{\mathrm{QP},*}_{ij} = m^*_{ij}(1+\lambda_{ij})$, where m^*_{ij} represents the G_0W_0 effective mass. On the basis of these definitions, from Eq. (9) we can derive the following relation for λ_{ij}:

$$\frac{1}{1+\lambda_{ij}} = 1 + \frac{m^*_{ij}}{\hbar^2} \frac{\partial^2}{\partial k_i \partial k_j} \sum_{\nu} \mathrm{Re}\Sigma^{\nu}_{n\mathbf{k}}(\varepsilon_{n\mathbf{k}}). \tag{11}$$

When λ_{ij} is small, as in the present case, $(1+\lambda_{ij})^{-1} \approx 1 - \lambda_{ij}$. It follows that λ_{ij} can be approximately written as the sum of the contribution from different phonon branches, i.e. $\lambda_{ij} \approx \sum_{\nu} \lambda^{\nu}_{ij}$, where λ^{ν}_{ij} represents the mass enhancement calculated when only the contribution from the phonon branch ν is included:

$$\lambda^{\nu}_{ij} = -\frac{m^*_{ij}}{\hbar^2} \frac{\partial^2}{\partial k_i \partial k_j} \left[\mathrm{Re}\Sigma^{\nu}_{n\mathbf{k}}(\varepsilon_{n\mathbf{k}})\right]. \tag{12}$$

Substitution of Eq. (10) into Eq. (12), we can furthur

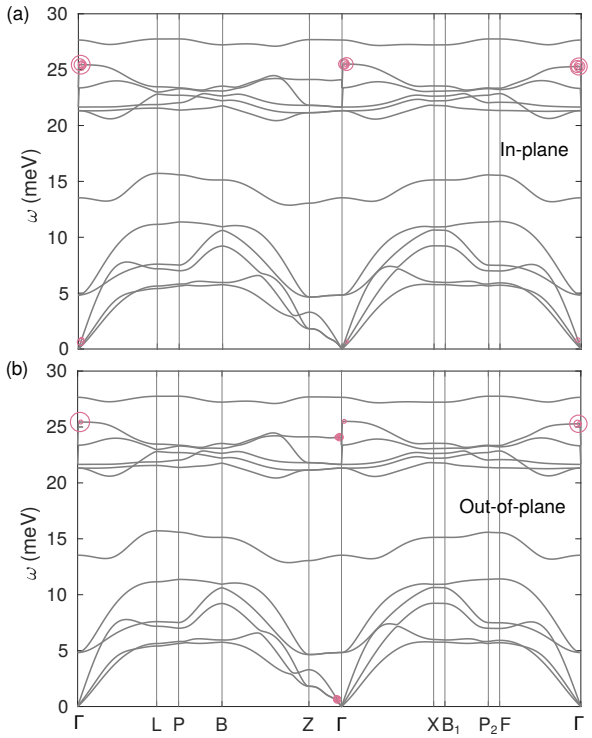

FIG. 4. Decomposition of phonon-mode contribution to the effective mass enhancement of the electron carriers in InSe, calculated within the Rayleigh-Schrödinger perturbation theory at 300 K. (a) and (b) represent the results for in-plane and out-of-plane effective mass enhancement respectively. The size of magenta circles superimposed on the phonon spectra is proportional to the relative contribution of each phonon mode. The results show that the dominant contributions to the effective mass enhancement originate from the Fröhlich optical phonons and long-wavelength acoustic phonons.

write λ_{ij} as:

$$\lambda_{ij} \approx \sum_{\nu} \int \frac{d\mathbf{q}}{\Omega_{\mathrm{BZ}}} \left(-\frac{m^*_{ij}}{\hbar^2}\right) \frac{\partial^2}{\partial k_i \partial k_j} \sum_m \Bigg[|g_{mn\nu}(\mathbf{k},\mathbf{q})|^2 \times \sum_{\pm} \frac{n_{\mathbf{q}\nu} + (1 \pm [2 f_{m\mathbf{k}+\mathbf{q}} - 1])/2}{\varepsilon_{n\mathbf{k}} - \varepsilon_{m\mathbf{k}+\mathbf{q}} \pm \hbar\omega_{\mathbf{q}\nu}} \Bigg]. \tag{13}$$

We can then compare the contributions of different phonon modes $\mathbf{q}\nu$ to the effective mass enhancement λ_{ij} of electron $n\mathbf{k}$ by comparing the following quantity $\Theta^{\mathbf{q}\nu}_{ij}(\varepsilon_{n\mathbf{k}})$ between different phonon modes:

$$\Theta^{\mathbf{q}\nu}_{ij}(\varepsilon_{n\mathbf{k}}) = -|\mathbf{q}|^2 \frac{\partial^2}{\partial k_i \partial k_j} \sum_m \Bigg[|g_{mn\nu}(\mathbf{k},\mathbf{q})|^2 \sum_{\pm} \frac{n_{\mathbf{q}\nu} + (1 \pm [2 f_{m\mathbf{k}+\mathbf{q}} - 1])/2}{\varepsilon_{n\mathbf{k}} - \varepsilon_{m\mathbf{k}+\mathbf{q}} \pm \hbar\omega_{\mathbf{q}\nu}} \Bigg], \tag{14}$$

where $|\mathbf{q}|^2$ takes into account the difference in volume elements in $\mathbf{q}$ space within spherical approximation. The calculated phonon dispersion of γ-InSe is shown in Fig. 3(a).

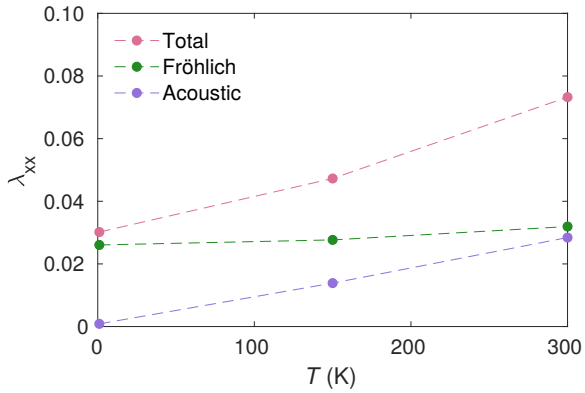

FIG. 5. The temperature dependence of phonon-branch contributions to the effective mass enhancement of electron carriers in InSe, calculated within the Rayleigh-Schrödinger perturbation theory. We plot the in-plane effective mass enhancement (λ_{xx}) as a function of temperature (T) and the respective contributions of the Fröhlich and acoustic phonons to the mass enhancement. Similar results are found for the out-of-plane effective mass enhancement.

In Fig. 4 we overlap the relative values of $\Theta^{\mathbf{q}\nu}_{ij}$ for the electron at conduction band minimum at 300 K on the calculated phonon spectrum of γ-InSe. The values of $\Theta^{\mathbf{q}\nu}_{ij}$, which are proportional to the size of the superimposed circles, correspond to the relative contributions of different phonon modes $\mathbf{q}\nu$ to the effective mass enhancement λ_{ij}. In the plots we only show circles when $\Theta^{\mathbf{q}\nu}_{ij} > 30$ meV. The results indicate that the main contributions to the EPI-induced effective mass renormalization at 300 K originate from long-wavelength polar longitudinal optical (LO) phonons, namely the Fröhlich optical phonons, as well as long-wavelength acoustic phonons. The Fröhlich optical phonons, whose energies are around 25 meV, are indicated on the phonon spectrum of γ-InSe in Fig. 3(a). A representative pattern of the atomic displacements corresponding to the in-plane Fröhlich phonons is shown in Fig. 3(b).

We have further investigated the temperature dependence of the different phonon-branch contributions to effective mass enhancement by calculating λ^{ν}_{ij} as a function of temperature. In calculating λ^{ν}_{ij} using Eq. (10) and Eq. (12), we converge the self-energy $\mathrm{Re}\Sigma^{\nu}_{n\mathbf{k}}(\varepsilon_{n\mathbf{k}})$ by carrying out the Brillouin-zone integration over $\mathbf{q}$ according to a random Cauchy distribution centered at Γ point, as described in Sec. II C. Fig. 5 shows that the main contribution to the EPI-induced in-plane effective mass renormalization at low temperature originates from the interaction of electrons with the Fröhlich optical phonons, whereas the acoustic contribution exhibits a more rapid increase with respect to temperature than the Fröhlich contribution and becomes comparable to the LO contribution at room temperature. This trend can be rationalized by the smaller energies of the acoustic phonons as compared to those of the Fröhlich phonons, leading

TABLE IV. The calculated high-frequency dielectric constants ε_∞, static dielectric constants ε_0, and Born effective charges $\mathcal{Z}^*$ of γ-InSe along both the in-plane and out-of-plane directions. The results are obtained from calculations based on density functional perturbation theory.

	ε_∞	ε_0	$\mathcal{Z}^*$(In)	$\mathcal{Z}^*$(Se)
In-plane	8.8	11.2	2.39	-2.39
Out-of-plane	11.6	12.2	1.18	-1.18

TABLE V. The bandgap (E_g), in-plane effective mass (m^*_{xx}), and out-of-plane effective mass (m^*_{zz}) of γ-InSe obtained from DFT with different exchange-correlation functionals. The effective masses are measured in units of m_e, which represents the rest mass of an electron.

exchange-correlation functional	E_g (eV)	m^*_{xx}/m_e	m^*_{zz}/m_e
LDA	0.21	0.103	0.024
PBEsol	0.32	0.109	0.036
PBE	0.42	0.117	0.045

to a more rapid increase of the phonon occupation number with temperature and the resulting enhanced renormalization of the carrier effective mass. Similar phonon-branch contributions are found for the out-of-plane effective mass enhancement.

The significant contribution of the Fröhlich interaction to the effective mass enhancement near room temperature motivates us to quantify the strength of this interaction. For this purpose we employ the simple Fröhlich model, which considers an isotropic polar medium in which electrons with parabolic band dispersion and effective mass m^* interact with polar LO phonons with a constant energy $\hbar\omega_0$ [40]. Within this model, the strength of the Fröhlich interaction can be quantified using a dimensionless Fröhlich coupling constant α, whose expression is given by

$$\alpha = \frac{e^2}{4\pi\epsilon_0\hbar}\left(\frac{m^*}{2\hbar\omega_0}\right)^{1/2}\left(\frac{1}{\varepsilon_\infty}-\frac{1}{\varepsilon_0}\right). \qquad (15)$$

Here, ε_∞ and ε_0 represent the high-frequency and static dielectric constants respectively. Although bulk γ-InSe is not a fully isotropic system, the calculated in- and out-of-plane band effective masses, as listed in Table III, as well as the calculated dielectric constants listed in Table IV, do not exhibit significant directional anisotropy. Therefore the isotropic Fröhich model can still provide useful insight into the strength of Fröhlich interaction in this system.

Using the calculated in-plane effective mass $m^*_{xx} = 0.12$, the Fröhlich phonon energy $\hbar\omega_0 = 25$ meV, and the in-plane dielectric constants $\varepsilon_\infty = 8.8$ and $\varepsilon_0 = 11.2$, we obtain $\alpha = 0.2$. This value places the Fröhlich interaction in InSe in the weak coupling regime [40]. In this regime, the effective mass enhancement λ is related to α as $\lambda \approx \alpha/6$ [41], from which we obtain $\lambda \approx 0.033$. This value is very close to the calculated Fröhlich contribution to the in-plane mass enhancement of InSe within the Rayleigh-Schrödinger perturbation theory, as seen from Fig. 5. We additionally calculate the value of α using the measured in-plane dielectric constants of InSe [42]: $\varepsilon_\infty = 7.8$ and $\varepsilon_0 = 10.9$. The corresponding value of α is 0.29, in close agreement with the *ab initio* result. These results indicate that the small effective mass of the conduction band electrons, the reasonably strong electronic screening as seen from ε_∞, and the weak lattice polarizability as reflected in the small difference between ε_0 and ε_∞, all contribute to the weak Fröhlich coupling strength and the small EPI-induced electron mass enhancement.

IV. DISCUSSION

The DFT electron effective masses of bulk γ-InSe calculated at LDA level are $0.103m_e$ and $0.024m_e$ in the in-plane and out-of-plane directions respectively. After including both electron-electron and electron-phonon renormalization, the in- and out-of-plane electron effective masses separately increase to $0.123m_e$ and $0.089m_e$. For comparison, the corresponding experimentally measured electron effective masses of InSe are $0.14m_e$ and $0.08m_e$, respectively [11]. Although the calculation and experimental results are quite close, the calculation results represent an underestimate of 12% for the in-plane and an overestimate of 11% for the out-of-plane experimental effective masses.

Since we found that many-body renormalization of electron effective masses are dominated by electron-electron effect, one possible origin of the discrepancy between calculation and experiment could be the dependence of single-shot G_0W_0 effective masses on the DFT starting point for many-body perturbation calculations. It is well established that the Kohn-Sham eigenvalues and eigenstates used as the DFT starting point for G_0W_0 calculations could affect the G_0W_0 quasiparticle energies and hence the effective masses [43, 44]. In our study, we use the LDA exchange-correlation functional as the DFT starting point. We have additionally calculated the DFT effective masses using the PBEsol [45] and PBE [46] exchange-correlation functionals, using the same atomic structure of LDA. The results, listed in Table V, indicate that the exchange-correlation functional employed in the calculations affects both the in- and out-of-plane effective masses at DFT level. Such difference in the DFT starting point could in turn influence the G_0W_0 effective masses. For example, given that the in-plane effective mass calculated at DFT level using the PBE exchange-correlation functional is $0.117m_e$ compared to the value of $0.103m_e$ calculated using LDA, the use of PBE exchange-correlation functional as the DFT starting point is likely to bring the G_0W_0 effective mass closer to the experimental value of $0.14m_e$. However, regardless of the DFT starting point, the conclusions of our study, that electron-electron effects dominate

over electron-phonon effects in many-body renormalization, and that the many-body corrections are anisotropic, would remain robust. We also note that the sensitivities of GW effective mass on the DFT starting point can be mitigated by employing a self-consistent approach by iteratively updating the Green's function G and/or the screened Coulomb potential W [43, 47, 48]. Detailed investigation of the effect of self-consistency on the GW effective mass of InSe could be the subject of future study.

For the temperature dependence of electron effective mass, in addition to the change in effective mass renormalization due to the change of phonon occupation number, which affects the strength of electron-phonon interaction, we note that the change of lattice constants due to thermal expansion could also affect the electron effective mass. The thermal expansion coefficients of InSe have been experimentally measured by Belenkii *et al.* [49]. Being a layered material, the thermal expansion coefficients of InSe are anisotropic. In the temperature range from 100 K to room temperature, the in- and out-of-plane thermal expansion coefficients of InSe are both around 1×10^{-5} K^{-1}, with the out-of-plane coefficients about two times larger than the in-plane coefficients. On the basis of the experimental data in Ref. [49], we estimate that the lattice-constant change of InSe from zero to room temperature is less than 0.25% in the in-plane direction, and less than 0.5% in the out-of-plane direction. We note that the experimental electron effective masses in Ref. [11] were measured at 94 K, whereas our calculations employ the experimental lattice constants measured at room temperature. Hence, the lattice constants corresponding to the temperature at which the electron effective masses are measured should be smaller than those we use for DFT calculations, by an amount less than 0.5%.

To understand the effects of thermal expansion on the electron effective mass of InSe, we first apply a -0.5% of strain along the c axis of the crystal (the z direction in Fig. 1), while keeping the in-plane lattice constants the same. The DFT electron effective mass calculated in the in-plane direction changes slightly, from 0.103 to 0.105, while the out-of-plane electron effective mass decreases from 0.022 to 0.019. On the other hand, if we apply a -0.5% of strain on the experimental in-plane lattice constants, while keeping the c lattice constant the same, the in-plane electron effective mass increases marginally from 0.103 to 0.104, while the out-of-plane effective mass increases from 0.022 to 0.028. The results indicate that the in-plane electron effective mass of InSe is relatively insensitive to thermal contraction/expansion below room temperature. For out-of-plane electron effective mass, the effect of lattice constant change along the in- and out-of-plane directions due to thermal expansion counterbalances each other, which reduces the magnitude of possible effective mass change. Indeed, when applying a -0.5% of strain along the c axis and a -0.25% of in-plane strain simultanously, which approximates the decrease of experimental lattice constants from 300 K to 94 K, we find that the DFT in-plane electron effective mass only varies from 0.103 to 0.104, while the out-of-plane electron effective mass barely increases from 0.022 to 0.023. Therefore, the effects of thermal expansion on the electron effective mass of InSe are insignificant.

V. CONCLUSIONS

In conclusion, using state-of-the-art computational methods, we have presented a comprehensive study of the many-body renormalization of the electron effective mass in γ-InSe. The EEI- and EPI-renormalized effective electron mass are around $0.12m_e$ and $0.09m_e$ in the in- and out-of-plane direction respectively, in good agreement with the measured data of $0.14m_e$ and $0.08m_e$, respectively [11]. We find that the EEI-induced electron effective mass renormalization has a strong directional anisotropy, which we explain in terms of the symmetry of the band-edge wavefunctions. We also find weak EPI-induced mass renormalization, which mainly originates from the weak Fröhlich interaction in the system. These results provide insight into the nature and strength of many-body interactions in InSe. Given the broad impact of carrier effective mass on the properties of semiconductors, the results presented in this study will be useful for designing electronic and optoelectronic devices based on InSe as well as other monochalcogenide semiconductors with similar atomic and electronic structure, such as GaS and GaSe [18].

VI. ACKNOWLEDGEMENTS

The authors acknowledge support from the European Unions Horizon 2020 research and innovation programme under the Marie Skłodowska-Curie grant agreement No. 743580. We acknowledge the use of the University of Oxford Advanced Research Computing (ARC) facility, the Cambridge Service for Data Driven Discovery (Grant No. EP/P020259/1), and the UK Materials and Molecular Modelling Hub. W.L. acknowledges the support by foundation of Westlake University. Work by F.G. at UT was supported by the U.S. Department of Energy (DOE), Office of Science, Basic Energy Sciences (BES) under Award DE-SC0020129. The authors thanks S. Poncé for helpful discussions. Structural models were rendered using VESTA [50].

[1] D. A. Bandurin, A. V. Tyurnina, G. L. Yu, A. Mishchenko, V. Zólyomi, S. V. Morozov, *et al.*, High electron mobility, quantum hall effect and anomalous op-

tical response in atomically thin InSe, Nat. Nanotechnol. **12**, 223 (2017).
[2] W. Feng, W. Zheng, W. Cao, and P. Hu, Back gated multilayer InSe transistors with enhanced carrier mobilities via the suppression of carrier scattering from a dielectric interface, Adv. Mater. **26**, 6587 (2014).
[3] S. Sucharitakul, N. J. Goble, U. R. Kumar, R. Sankar, A. A. Bogorad, F.-C. Chou, Y. Chen, and X. P. A. Gao, Intrinsic electron mobility exceeding 10^3 $cm^2/(Vs)$ in multilayer InSe FETs, Nano Lett. **15**, 3815 (2015).
[4] S. J. Magorrian, V. Zólyomi, and V. I. Fal'ko, Electronic and optical properties of two-dimensional InSe from a DFT-parametrized tight-binding model, Phys. Rev. B **94**, 245431 (2016).
[5] S. J. Magorrian, V. Zólyomi, and V. I. Fal'ko, Spin-orbit coupling, optical transitions, and spin pumping in monolayer and few-layer InSe, Phys. Rev. B **96**, 195428 (2017).
[6] S. J. Magorrian, A. Ceferino, V. Zólyomi, and V. I. Fal'ko, Hybrid $\mathbf{k}\cdot\mathbf{p}$ tight-binding model for intersubband optics in atomically thin inse films, Phys. Rev. B **97**, 165304 (2018).
[7] D. J. Terry, V. Zólyomi, M. Hamer, A. V. Tyurnina, D. G. Hopkinson, A. M. Rakowski, S. J. Magorrian, N. Clark, Y. M. Andreev, O. Kazakova, K. Novoselov, S. J. Haigh, V. I. Fal'ko, and R. Gorbachev, Infrared-to-violet tunable optical activity in atomic films of GaSe, InSe, and their heterostructures, 2D Mater. **5**, 041009 (2018).
[8] M. J. Hamer, J. Zultak, A. V. Tyurnina, V. Zólyomi, D. Terry, A. Barinov, A. Garner, J. Donoghue, A. P. Rooney, V. Kandyba, A. Giampietri, A. Graham, N. Teutsch, X. Xia, M. Koperski, S. J. Haigh, V. I. Fal'ko, R. V. Gorbachev, and N. R. Wilson, Indirect to direct gap crossover in two-dimensional InSe revealed by angle-resolved photoemission spectroscopy, ACS Nano **13**, 2136 (2019).
[9] J. Zultak, S. Magorrian, M. Koperski, A. Garner, M. J. Hamer, E. Tovari, K. S. Novoselov, A. Zhukov, Y. Zou, N. R. Wilson, S. J. Haigh, A. Kretinin, V. I. Fal'ko, and R. Gorbachev, Ultra-thin van der Waals crystals as semiconductor quantum wells, arXiv e-prints , arXiv:1910.04215 (2019).
[10] W. Li, S. Poncé, and F. Giustino, Dimensional crossover in the carrier mobility of two-dimensional semiconductors: The case of InSe, Nano Lett. **19**, 1774 (2019).
[11] E. Kress-Rogers, R. J. Nicholas, J. C. Portal, and A. Chevy, Cyclotron resonance studies on bulk and two-dimensional conduction electrons in InSe, Solid State Commun. **44**, 379 (1982).
[12] P. Hohenberg and W. Kohn, Inhomogeneous electron gas, Phys. Rev. **136**, B864 (1964).
[13] D. M. Ceperley and B. J. Alder, Ground state of the electron gas by a stochastic method, Phys. Rev. Lett. **45**, 566 (1980).
[14] J. P. Perdew and Y. Wang, Accurate and simple analytic representation of the electron-gas correlation energy, Phys. Rev. B **45**, 13244 (1992).
[15] L. Hedin and S. Lundqvist, Effects of electron-electron and electron-phonon interactions on the one-electron states of solids, in *Solid State Physics* (Elsevier, 1970) pp. 1–181.
[16] M. S. Hybertsen and S. G. Louie, Electron correlation in semiconductors and insulators: Band gaps and quasiparticle energies, Phys. Rev. B **34**, 5390 (1986).
[17] F. Giustino, Electron-phonon interactions from first principles, Rev. Mod. Phys. **89**, 015003 (2017).
[18] O. Madelung, *Semiconductors: Data Handbook* (Springer-Verlag Berlin Heidelberg, 2004).
[19] A. Aryasetiawan and O. Gunnarsson, The GW method, Rep. Prog. Phys. **61**, 237 (1998).
[20] G. Onida, L. Reining, and A. Rubio, Electronic excitations: density-functional versus many-body green's-function approaches, Rev. Mod. Phys. **74**, 601 (2002).
[21] H. Y. Fan, Temperature dependence of the energy gap in semiconductors, Phys. Rev. **82**, 900 (1951).
[22] A. B. Migdal, Interaction between electrons and lattice vibrations in a normal metal, Sov. Phys. JETP **7**, 996 (1958).
[23] P. Giannozzi, O. Andreussi, T. Brumme, O. Bunau, M. Buongiorno Nardelli, M. Calandra, *et al.*, Advanced capabilities for materials modelling with Quantum ESPRESSO, J. Phys. Condens. Matter **29**, 465901 (2017).
[24] J. Rigoult, A. Rimsky, and A. Kuhn, Refinement of the 3R γ-indium monoselenide structure type, Acta Cryst. B **36**, 916 (1980).
[25] N. Troullier and J. Martins, Efficient pseudopotentials for plane-wave calculations, Phys. Rev. B **43**, 1993 (1991).
[26] A. Marini, C. Hogan, M. Grüning, and D. Varsano, yambo: An ab initio tool for excited state calculations, Comput. Phys. Commun. **180**, 1392 (2009).
[27] S. L. Adler, Quantum theory of the dielectric constant in real solids, Phys. Rev. **126**, 413 (1962).
[28] R. W. Godby and R. J. Needs, Metal-insulator transition in kohn-sham theory and quasiparticle theory, Phys. Rev. Lett. **62**, 1169 (1989).
[29] F. Bruneval and X. Gonze, Accurate GW self-energies in a plane-wave basis using only a few empty states: Towards large systems, Physical Review B **78**, 10.1103/physrevb.78.085125 (2008).
[30] A. A. Mostofi, J. R. Y., G. Pizzi, Y.-S. Lee, I. Souza, D. Vanderbilt, and N. Marzari, An updated version of wannier90: A tool for obtaining maximally-localised Wannier functions, Comput. Phys. Commun. **185**, 2309 (2014).
[31] F. Hüser, T. Olsen, and K. S. Thygesen, How dielectric screening in two-dimensional crystals affects the convergence of excited-state calculations: Monolayer mos_2, Phys. Rev. B **88**, 245309 (2013).
[32] D. Y. Qiu, F. H. da Jornada, and S. G. Louie, Screening and many-body effects in two-dimensional crystals: Monolayer mos_2, Phys. Rev. B **93**, 235435 (2016).
[33] S. Poncé, E. R. Margine, C. Verdi, and F. Giustino, EPW: Electron–phonon coupling, transport and superconducting properties using maximally localized wannier functions, Comput. Phys. Commun. **209**, 116 (2016).
[34] F. Giustino, M. L. Cohen, and S. G. Louie, Electron-phonon interaction using Wannier functions, Phys. Rev. B **76**, 165108 (2007).
[35] S. Baroni, S. de Gironcoli, A. Dal Corso, and P. Giannozzi, Phonons and related crystal properties from density-functional perturbation theory, Rev. Mod. Phys. **73**, 515 (2001).
[36] C. Verdi and F. Giustino, Fröhlich electron-phonon vertex from first principles, Phys. Rev. Lett. **115**, 176401 (2015).
[37] M. Schlipf, S. Poncé, and F. Giustino, Carrier lifetimes and polaronic mass enhancement in the hybrid halide

perovskite $CH_3NH_3PbI_3$ from multiphonon fröhlich coupling, Phys. Rev. Lett. **121**, 086402 (2018).
[38] P. Y. Yu and M. Cardona, *Fundamentals of Semiconductors: Physics and Materials Properties* (Springerk, Berlin, 2010).
[39] T. Inui, Y. Tanabe, and Y. Onodera, *Group Theory and Its Applications in Physics*, Vol. 78 (Springerk, Berlin, 1996).
[40] G. D. Mahan, *Many-Particle Physics* (Springer, 2000).
[41] J. T. Devreese and A. S. Alexandrov, Fröhlich polaron and bipolaron: recent developments, Rep. Prog. Phys. **72**, 066501 (2009).
[42] N. Kuroda and Y. Nishina, Resonance raman scattering study on exciton and polaron anisotropies in InSe, Solid State Commun. **34**, 481 (1980).
[43] M. van Schilfgaarde, T. Kotani, and S. Faleev, Quasiparticle self-consistent *GW* theory, Phys. Rev. Lett. **96**, 226402 (2006).
[44] F. Fuchs, J. Furthmüller, F. Bechstedt, M. Shishkin, and G. Kresse, Quasiparticle band structure based on a generalized kohn-sham scheme, Phys. Rev. B **76**, 115109 (2007).
[45] J. P. Perdew, A. Ruzsinszky, G. I. Csonka, O. A. Vydrov, G. E. Scuseria, L. A. Constantin, X. Zhou, and K. Burke, Restoring the density-gradient expansion for exchange in solids and surfaces, Phys. Rev. Lett. **100**, 136406 (2008).
[46] J. P. Perdew, K. Burke, and M. Ernzerhof, Generalized gradient approximation made simple, Phys. Rev. Lett. **77**, 3865 (1996).
[47] M. Shishkin and G. Kresse, Self-consistent *gw* calculations for semiconductors and insulators, Phys. Rev. B **75**, 235102 (2007).
[48] M. R. Filip and F. Giustino, *GW* quasiparticle band gap of the hybrid organic-inorganic perovskite $CH_3NH_3PbI_3$: Effect of spin-orbit interaction, semicore electrons, and self-consistency, Phys. Rev. B **90**, 245145 (2014).
[49] G. L. Belenkii, E. Y. Salaev, R. A. Suleimanov, N. A. Abdullaev, and V. Y. Shteinshraiber, The nature of negative linear expansion in layer crystals C, BN, GaS, GaSe and InSe, Solid State Commun. **53**, 967 (1985).
[50] K. Momma and F. Izumi, VESTA: a three-dimensional visualization system for electronic and structural analysis, J. Appl. Cryst. **41**, 653 (2008).